MEMS Kinematics by Super-Resolution Fluorescence Microscopy

Craig D. McGray, Samuel M. Stavis, Joshua Giltinan, Eric Eastman, Samara Firebaugh, Jenelle Piepmeier, Jon Geist, and Michael Gaitan

Abstract—Super-resolution fluorescence microscopy is used for the first time to study the nanoscale kinematics of a MEMS device in motion across a surface. A device under test is labeled with fluorescent nanoparticles that form a microscale constellation of near-ideal point sources of light. The constellation is imaged by widefield epifluorescence microscopy, and the image of each nanoparticle is fit to a Gaussian distribution to calculate its position. Translations and rotations of the device are measured by computing the rigid transform that best maps the constellation from one image to the next. This technique is used to measure the stepwise motion of a scratch drive actuator across each of 500 duty cycles with 0.13-nm localization precision, 1.85-nm displacement uncertainty, and 100-μrad orientation uncertainty for a constellation diameter of 15 μm. This novel measurement reveals acute aperiodic variations in the step size of the actuator, which have been neither previously observed nor predicted by any of the published models of the operation of the device. These unexpected results highlight the importance of super-resolution fluorescence microscopy to the measurement of MEMS kinematics, which will have broad impact in fundamental investigations of surface forces, wear, and tribology in MEMS and related applications. [2012-0149]

Index Terms—Fluorescence microscopy, kinematics, MEMS, scratch drive, super-resolution.

I. INTRODUCTION

MEASUREMENTS of the kinematics of MEMS devices can be challenging because the devices are inherently small and the characteristic motions of the devices are often many orders of magnitude smaller. As a result, assessments of

device kinematics are often limited by lumped 1-D models or by observations of device motions that have been aggregated over tens, hundreds, or thousands of operating cycles [1]–[3]. In the few cases that individual nanoscale motion cycles of microscale devices have been resolved, the results have been very informative regarding device operation, wear, reliability, and underlying surface tribology [4], [5]. Therefore, advancing the state of the art in the measurement of MEMS kinematics at small length scales is a promising path toward a better understanding of device operating mechanisms and better control of performance and reliability [6].

MEMS kinematics are especially difficult to measure when the plane of device motion is parallel to the plane of the substrate on which the device is operated [1], [7]–[9]. Such is the case for many varieties of accelerometers, resonators, gyroscopes, linear actuators, and rotary motors. Existing techniques for measuring the in-plane motions of such devices include magnetomotive [10] and capacitive [11] sensing, optical probe-based techniques [12], laser Doppler vibrometry (LDV) [13], and approaches based on computer microvision [7], [9], [14], [15].

Techniques based on magnetomotive, capacitive, and optical probes allow device displacements to be measured with high resolution at up to gigahertz frequencies. However, as single-point measurements, these techniques inherently measure the lumped effect of device motion on the sensed quantity and are typically uniaxial, treating either translational or rotational motion, but not both. In practice, the assumption of a single fixed axis of motion is approximate. LDV can be performed at a single point so that transient motions at that point can be measured to gigahertz frequencies, or the probed point can be scanned so that periodic out-of-plane translations and rotations can be measured across entire surfaces. However, in-plane LDV measurements are problematic for many MEMS devices because the often specular surfaces of these devices scatter very little light within the motion plane.

In-plane motion metrology based on computer microvision is particularly promising, enabling measurements to be made across the full field of view of an optical microscope with a full three degrees of freedom: translation in the x-axis, translation in the y-axis, and rotation in θ. Moreover, surface features of the device under test can provide sufficient contrast for super-resolution analysis. Previously, this contrast has been achieved by etching gratings or arrays of circles directly into the device material. Such an approach requires that the device fabrication process incorporate the test features that enable the measurement, and the contrast depends on structural alterations
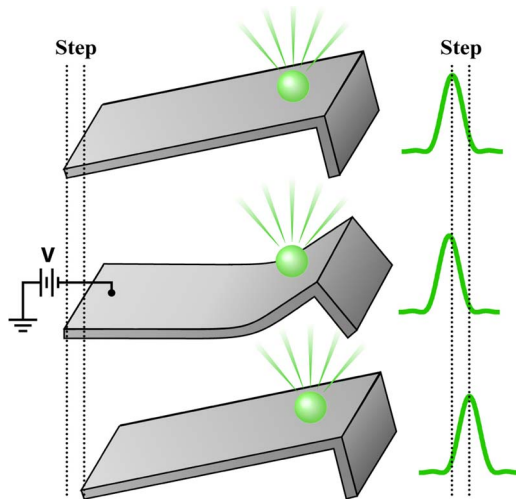
Fig. 1. Super-resolution fluorescence microscopy of the nanoscale motion of a microscale scratch drive actuator [2]. When a voltage V is applied cyclically, the actuator moves forward in the stepwise manner illustrated. Fluorescent nanoparticles deposited onto the actuator appear as point sources of light in fluorescence micrographs of the actuator, creating Airy patterns in the collected images in the case of ideal optics. Fitting these images by nonlinear regression allows measurement of the actuator displacement to be performed to within an overall empirical measurement uncertainty of 1.85 nm. The resolution of this method allows measurement of individual steps of the actuator, which typically ranged between 20 and 80 nm in these experiments.

in the device that may need to be very pronounced as to effect mechanical performance.

As demonstrated in this paper, computer microvision techniques can be enhanced by depositing fluorescent sources of light onto the surface of the device under test to provide the image contrast necessary for super-resolution image analysis. If the size of a fluorescent indicator is beneath the Rayleigh resolution of the imaging microscope, then its image appears as the point spread function of the microscope, which in the case of ideal optics is an Airy pattern. The point spread function can be fit to a model such as a Gaussian function, the center of which can be then calculated by nonlinear regression [16]. These and other related techniques have been developed extensively for imaging of biological processes at the microscale and nanoscale [17], as well as having been utilized for deformation and strain visualization [18]. As demonstrated in this paper, super-resolution fluorescence microscopy techniques can be used to provide three-degree-of-freedom full-field imaging of the motion of microscale solid-state devices with nanometer and submilliradian resolution. These techniques will be useful for fundamental studies of the kinematics, tribology, and reliability of a variety of small solid-state devices, with numerous applications in MEMS, NEMS, microrobotics, and nanomanufacturing. As a specific example that pertains to these topics, super-resolution fluorescence microscopy is used in this paper to measure the kinematics of a scratch drive actuator in motion across a surface.

A scratch drive actuator is a canonical MEMS device [19] used for microrobotic assembly and manipulation systems, where it offers high force output and can be operated with or without tethers [2], [3], [19], [20]. As illustrated in Fig. 1, it consists of a thin flexible plate with a bushing at one end. The actuator rests on an operating substrate that contains electrodes

insulated by a thin dielectric layer. When a voltage is applied between the substrate and the actuator plate, the plate is drawn into contact with the dielectric layer, pushing the bushing forward. Upon release of the accumulated charge, the actuator returns to its original shape, slightly in front of where it began. The distance traveled over such a cycle is known as the *step size*. By repeatedly cycling the voltage, the actuator can be moved forward in a stepwise manner. Typical dimensions of the actuator are on the order of 100 μm in width and 50 μm in length, with a plate thickness and a bushing height of 1–2 μm. The average step size is typically a few tens of nanometers.

The scratch drive actuator is a particularly relevant MEMS device for this first application of the measurement technique due to its nanoscale step size, its quasi-static operation, and its extensive publication history that has yet to produce consensus on the best model of the device mechanics. A number of groups have developed electromechanical models for the motion of the scratch drive [21]–[29] based on aggregate measurements of its step size, i.e., the average step size is derived from the total distance traveled by the device over many operating cycles. Such measurements have estimated an average step size that is three orders of magnitude smaller than the overall dimension of the scratch drive. However, there have been no experimental data reported on the range and distribution of the displacements or the rotations due to individual steps of a device in motion. In practice, the kinematics of scratch drive actuators are critically affected by the properties of the contacting surfaces. This is due to the sliding-contact-class operating mechanism of the device, which is particularly resistant to accurate modeling and prone to the broadest set of failure modes. The ability to measure discrete steps would facilitate a better understanding of the actuation method and, more generally, of the underlying surface forces and tribology. The motion of the scratch drive is not well suited to analysis by many established methods for nanoscale measurement. In contrast, super-resolution fluorescence microscopy is appropriate to both the scale of motion and the device structure.

To resolve the individual displacements and rotations of the scratch drive actuator, a device under test is labeled with fluorescent nanoparticles, as illustrated in Fig. 1. The nanoparticles are imaged by widefield epifluorescence microscopy, and the position of the device under test is probed by super-resolution analysis of the nanoparticle images.

II. MEASUREMENT METHOD

A. Fluorescent Nanoparticle Deposition

To employ super-resolution fluorescence microscopy to measure MEMS kinematics, the fluorescent indicators must be small enough that they resemble point sources on the image plane of the microscope and they must be selectively placed in such a way that they do not interfere with the operation of the device under test. To place small fluorescent indicators in this fashion, a microtargeted liquid deposition system is employed. The system consists of a glass micropipette that is charged by a pressurized reservoir of a dilute solution of fluorescent nanoparticles and targeted by a micromanipulator.
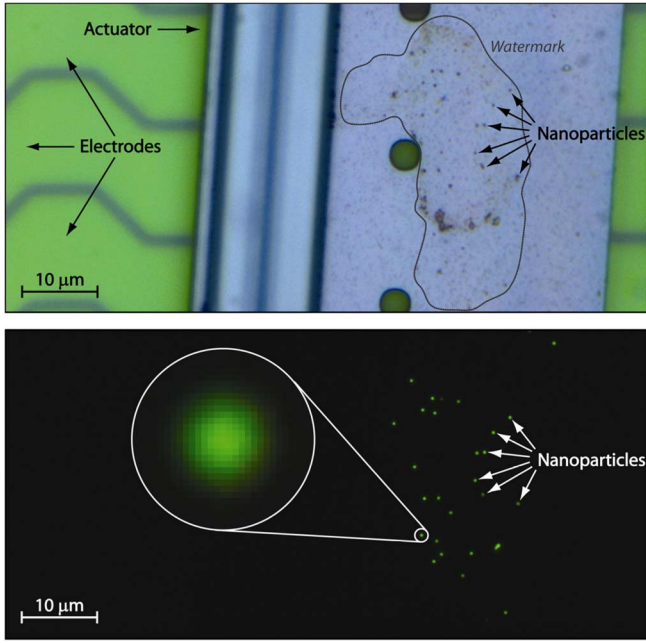
This article has been accepted for inclusion in a future issue of this journal. Content is final as presented, with the exception of pagination.

MCGRAY *et al.*: MEMS KINEMATICS BY SUPER-RESOLUTION FLUORESCENCE MICROSCOPY

3

Fig. 2. Scratch drive actuator labeled with a constellation of fluorescent nanoparticles. (*Top*) A bright-field micrograph shows the actuator resting on the substrate atop insulated electrodes through which electrical power is delivered capacitively. The nanoparticles are barely visible on the actuator. The watermark from the nanoparticle deposition process is outlined. (*Bottom*) A fluorescence micrograph shows only the nanoparticles. Since the diameters of the nanoparticles are beneath the Rayleigh resolution, each nanoparticle appears as a point source, creating an image of the 2-D point spread function of the microscope discretized by the digital CCD camera. (Inset) Image of a single nanoparticle with a measured green-channel pixel size of 46.82 ± 0.16 nm.

Surface tension forces acting on the liquid at the tip of the micropipette prevent fluid flow except when the tip is moved into contact with the device. Brief percussive tapping of the tip on the surface of the deposition target produces droplets with volumes on the order of 30 pL. These volumes are small enough that the liquid does not spill over to the edges and underside of the actuator where unintended deposition could cause device malfunction. As the droplets evaporate, the nanoparticles adhere to the device. A representative constellation of fluorescent nanoparticles deposited by this method is shown in Fig. 2.

B. Point Source Position Estimation

The position of each nanoparticle in a constellation can be determined through a super-resolution image analysis. The constellation is imaged with a charge-coupled device (CCD) digital camera mounted to a fluorescence microscope, and the image is stored for subsequent processing. Since the diameter of each fluorescent nanoparticle is less than the Rayleigh resolution limit, the image of each nanoparticle corresponds to the 2-D point spread function of the microscope. The position of each nanoparticle is estimated [16] by fitting the image of the nanoparticle to a 2-D Gaussian function with an offset for background noise. The position estimation operation can be performed with a three-step method, as follows. First, threshold and morphological operations are used to identify the image region in which each nanoparticle point spread function is

located. Second, the peak intensity of each identified region and the threshold boundary calculated in the first step are used to calculate a two-point analytical estimate of the point spread function. Third, least squares regression is used to find an optimal fit to the data using the analytical estimate from the second step as the initial estimate for nonlinear optimization.

C. Point Cloud Registration

The positions of all of the nanoparticles within a constellation together define a 2-D point cloud that provides a robust representation of both the position and the orientation of the device on which the constellation is deposited. This allows calculation of displacements and rotations of the device that occur in the time between the capture of two fluorescence micrographs. Displacements are calculated by the translation that maps the centroid of the first point cloud to that of the second. Rotations are calculated using the iterative closest point (ICP) algorithm [30], which simultaneously computes a registration mapping between the two point clouds along with the transform that converts the points in the first cloud to their analogs in the second. For simplicity, the translation component of the transform is computed from the point cloud centroids prior to execution of the ICP algorithm. This reduces the optimization problem embedded within the ICP algorithm to single-variable rotation.

III. MEASUREMENT RESULTS

A. Kinematics of the Scratch Drive Actuator

The above method was used to measure the nanometer and microradian scale kinematics of an untethered scratch drive actuator [3]. The actuator was operated at a stepping frequency of $1/3$ Hz while fluorescence micrographs were collected every 1.5 s so that two images were taken between each two successive steps. Displacements and rotations between successive frames taken before and after a step of the actuator were used to assess device motion, whereas displacements and rotations between pairs of frames taken without a step in between were used to assess measurement error and to allow calculation of the uncertainty of the position and orientation estimation method. Calculation of the measurement uncertainties is addressed in detail in Section III-B. A series of 1000 images was taken across a sequence of 500 actuator steps, and the position of the actuator was determined from the centroid of the point cloud defined by the nanoparticle positions. This process allowed construction of a detailed trajectory map of the motion of the actuator, as shown in Fig. 3. From a low-resolution perspective, the trajectory map is similar in appearance to previously reported scratch drive trajectories [20] and shows a smooth and consistent path that curves very slightly to the right as the actuator moves forward. The single-step resolution of this trajectory, however, allows a much more detailed inspection of the actuator motion than has been previously achieved, as shown in Fig. 3 (see the left inset). At this high resolution, it becomes clear that the motion is in fact markedly variable, with measured step sizes ranging from 66.1 nm down to 1.6 nm
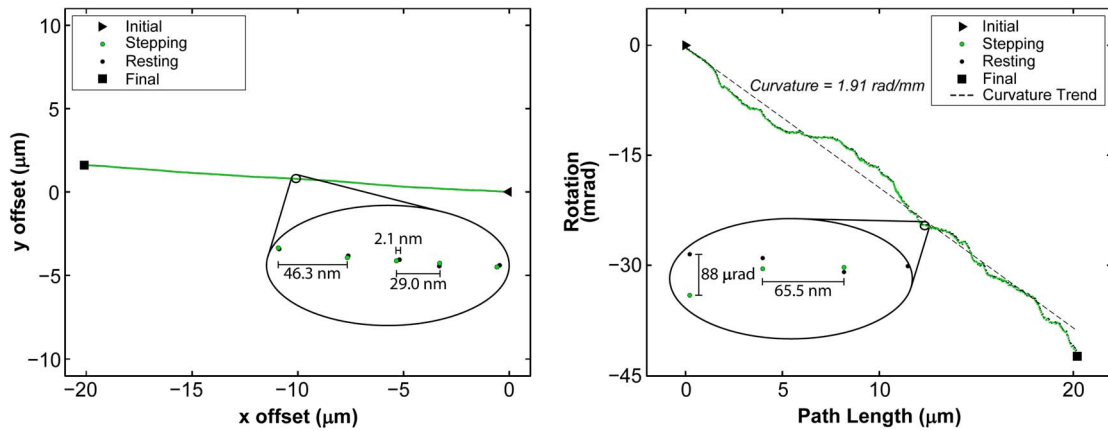
Fig. 3. Plots of a scratch drive actuator's (left) position and (right) orientation across 500 steps as measured by super-resolution fluorescence microscopy. Data points following time intervals in which the scratch drive was actuated (i.e., when it was stepped forward by an applied voltage change) are shown in green. Data following intervals when the actuator was not actuated (i.e., when it was in a resting state) are shown in black. The displacements and orientations observed between images taken when the actuator was in a resting state were used for an empirical analysis of the experimental measurement uncertainty. The 2.1-nm resting displacement identified in the inset is slightly higher than the mean of 1.6 nm over the full data set. The identified 88-μrad rotation during the rest cycle shown is slightly lower than the mean of 120 μrad for this data set.
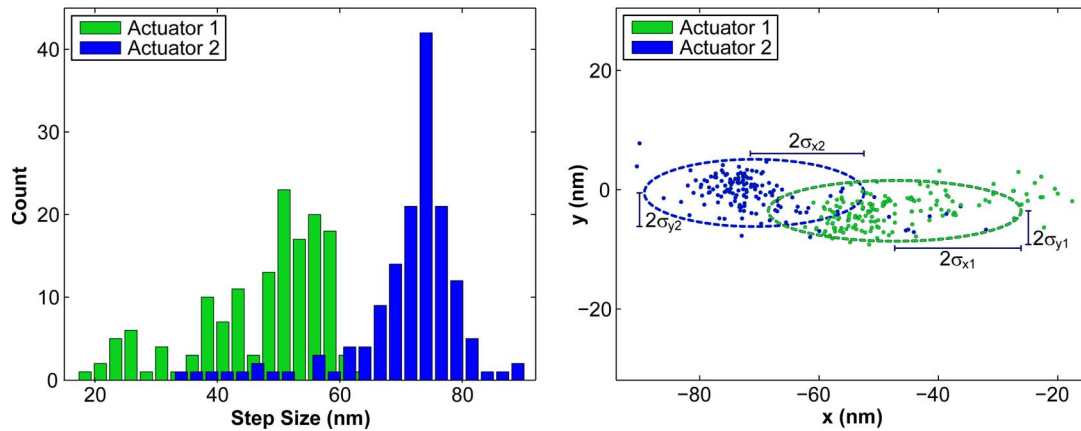

Fig. 4. Step-size distributions of two identically designed scratch drive actuators, shown as (left) distance histograms and (right) displacement scatter plots. Despite comparable standard deviations in step size ($\sigma_{x1}, \sigma_{y1}, \sigma_{x2}, \sigma_{y2}$), the two actuators exhibit qualitatively different distributions and distinct mean values. It is hypothesized that the variation in step size is due in part to differences in surface properties of the local contact interface between the actuator and the substrate.

within a single 500-step test run. The orientation trajectory of the actuator is shown in Fig. 3 (right). The motion curvature trend, which was barely discernible in the position trajectory, is now clearly visible and can be quantified by linear regression as -1.91 rad/mm.

The step-size distribution of the scratch drive actuator under test is shown in Fig. 4, and it is compared with the measured distribution of a second scratch drive actuator. The two actuators were of identical design and were operated with the same driving waveform on the same substrate. Temperature and humidity were controlled to ± 0.1 °C and ± 1.2 % RH, respectively. As the test run of the second actuator consisted of 150 steps, the first 150 steps of the first actuator were used in the comparison. This avoids any systematic bias that may occur due to wear or other performance degradation as a function of use. Histograms of step distances and scatter plots of single-step displacements are both shown. The mean step sizes over 150 cycles were 47.3 and 70.9 nm, with standard deviations of 10.6 and 8.8 nm for the first and second actuators, respectively. Existing models of the scratch drive actuator [2], [21]–[26],

[31] provide no basis for explaining such a large difference in the performance of the two devices. Rather, existing models treat step size as a constant function of the geometric and material properties of the actuator, the electrical thickness of the dielectric, the applied voltage, and in more recent models, the average coefficient of friction between the actuator and substrate materials. None of the existing models describe the step size as a statistical distribution, nor as depending upon local variations in the contact surface, nor in other ways that could explain the severe variation observed in the present measurement. However, time-series analysis of the fluorescence-based step-size measurements can provide some insight into this variation.

Fig. 5 shows the step size of each of the two actuators as a function of time, with 1.5 s between steps. The step size of Actuator 2 exceeds 61.7 nm 91% of the time, and the steps that fall beneath this threshold all fall within two contiguous sections of the graph. In each of these sections, the step size drops precipitously, bottoms out at 36 nm, and then climbs back above 61.7 nm into what can be considered the
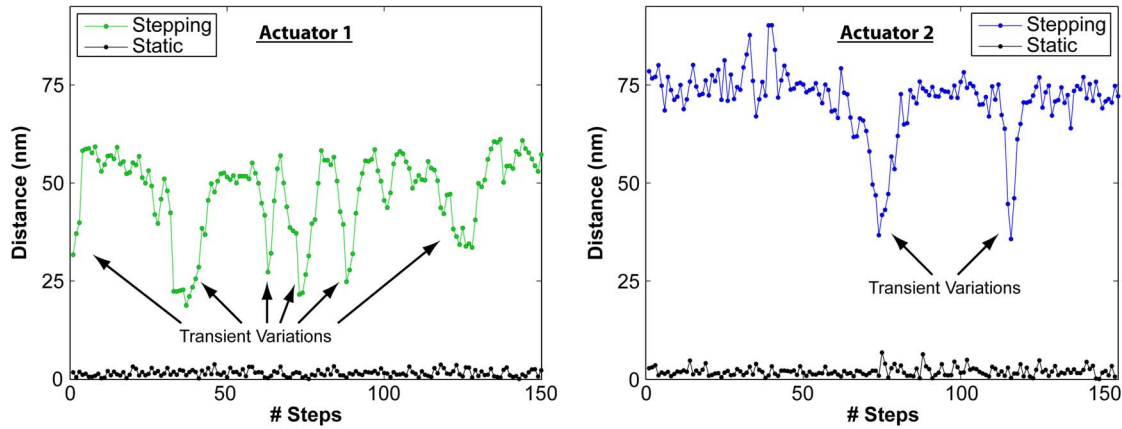
Fig. 5. Time-series step-size data for two identically designed scratch drives actuated by the same electrical waveform on the same substrate. For both actuators, temperature and humidity were controlled to ± 0.1 °C and $\pm 1.2\%$ RH, respectively. Green and blue data points represent the distance traveled in a single step of the first and second actuators, respectively. Each black data point represents the motion of an actuator measured between two frames when it was not stepping. These resting measurements are used to calculate displacement uncertainties, which demonstrate that the observed step-size variations are not an artifact of the measurement method. The time-series step-size data show aperiodic transient variations during which the step size decreases to less than half its nominal value and then recovers. It is hypothesized that these transient step-size variations occur in part due to asperities or contaminants on localized regions of the actuator–substrate interface. The observed transient variations are not predicted by existing actuator models [2], [21]–[26], [31], and they last for a total travel distance of less than a micrometer, making them difficult to detect using diffraction-limited optical microscopy without super-resolution image analysis. However, these transient variations are frequent enough to have a marked impact on the measured average step size of the actuator and would therefore confound measurements made using aggregate step-size data. In contrast, super-resolution fluorescence microscopy clearly reveals these motions.
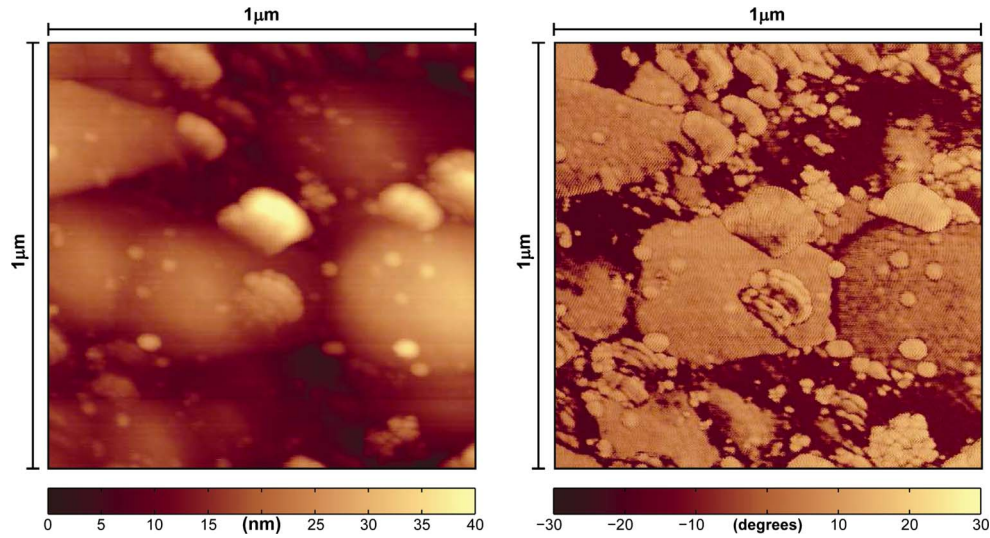

Fig. 6. Atomic force micrograph of a $1~\mu m \times 1~\mu m$ square of the substrate on which the scratch drive actuators were operated. (**Left**) The height channel of the micrograph shows asperities at multiple width scales having heights of up to 42.6 nm. (**Right**) The phase channel of the micrograph shows 51° of variation in the phase lag of the AFM cantilever probe. The phase lag conforms to a bimodal distribution with peaks at $-14°$ and $10°$, suggesting that two distinct materials are present on the operating substrate.

normal range of values. Actuator 1 shows six such transient variations, which occur so close together that it is not clear that the step size ever fully recovers before plunging into another transient.

Although the cause of these transient variations is not known, it is reasonable to hypothesize that the motion of the actuator relates in part to the local tribology of the operating landscape, which was characterized by atomic force microscopy (AFM). Fig. 6 shows a two-channel tapping-mode atomic force micrograph of the dielectric substrate. The first channel shows the AFM cantilever tip deflection as a function of lateral position, whereas the second channel shows the phase lag of the cantilever vibration relative to the stimulating waveform. Surface asperities having heights of up to ± 42.6 nm are visible

in the deflection channel. The phase channel exhibits variation of 51°, conforming to a bimodal distribution with peaks at $-14°$ and $10°$. The phase data are consistent with the presence of contaminants inhomogeneously adsorbed on the surface of the operating landscape.

Since the total distance that the actuator travels during one of these transient variations is on the order of a single wavelength of visible light, it would be difficult to observe these events by optical microscopy without super-resolution image analysis. Super-resolution fluorescence microscopy allows for the clear detection and measurement of such transient events, demonstrating the significant role that this class of technique may play in the kinematics and tribology of MEMS devices.

B. Measurement Uncertainty

Collection of two images at each position of the device under test allows determination of the uncertainty of the displacement measurement. Each pair of images provides two samples from the population of possible observed positions for each coordinate of the centroid of the nanoparticle constellation. From each such two-sample series, a mean and standard deviation can be extracted. From the set of 500 collected sample series, a pooled standard deviation of the measurement [32] can be extracted for the x-coordinate and another for the y-coordinate. These two pooled standard deviations describe statistical x- and y-axis uncertainties of the centroid position measurement. The standard uncertainty of the centroid displacement measurement is therefore the sum in quadrature of two x-axis position uncertainties and two y-axis position uncertainties. The standard uncertainty of the x-axis position was 0.91 nm. The standard uncertainty of the y-axis position was 0.94 nm. The combined standard uncertainty of the displacement measurement was 1.85 nm. Similarly, the pooled standard deviation of the orientation measured in each image pair is used to calculate the standard uncertainty of the stepwise rotation. The standard uncertainty of orientation was 70.7 μrad, and the combined standard uncertainty of the stepwise rotation measurement was 100 μrad.

C. Localization Precision

The standard uncertainties calculated from experimental data represent the empirical measurement uncertainties actually achieved in the specific experiment reported in this paper. The *localization precision* [33] values are much lower. These values reflect the displacement measurement uncertainties that are theoretically achievable with super-resolution fluorescence microscopy, given certain assumptions about the instrumentation. In an idealized model, the measurement uncertainty is limited by the total number of detected photons that form the image of the fluorescent nanoparticle, the number of detected background photons per pixel, the point spread function of the microscope, and the areal density of pixels over which the image is sampled.

The localization precision of the position of a fluorescent nanoparticle can be expressed as follows [33]:

$$L_P = \sqrt{\frac{16(\sigma^2 + a^2/12)}{9N} + \frac{8\pi b^2(\sigma^2 + a^2/12)}{a^2 N^2}} \qquad (1)$$

where σ is the standard deviation of the Gaussian approximation of the point spread function, a is the separation distance between adjacent pixels, b^2 is the expected number of background photons per pixel, and N is the total number of detected photons. The optical system described in this paper had a fitted Gaussian standard deviation of $\sigma = 160$ nm and a green-channel pixel separation of $a = 46.82$ nm after accounting for the GRGB Bayer color mosaic filter of the camera. With an exposure time of 400 ms, each fluorescent nanoparticle yielded an average of 257 000 detected photons with an average background intensity of $b^2 = 15$ detected photons per pixel. The

localization precision of the position of a single nanoparticle is therefore 0.42 nm.

The use of multiple fluorescent nanoparticles to determine the position of a MEMS device further improves the localization precision. When the position of the device is defined as the centroid of the positions of the nanoparticles, then the central limit theorem applies and the localization precision under an optics-limited model is

$$L_c = \sqrt{\frac{16(\sigma^2 + a^2/12)}{9N\eta} + \frac{8\pi b^2(\sigma^2 + a^2/12)}{a^2 N^2 \eta}} \qquad (2)$$

where L_c is the localization precision of the centroid position, and η is the number of nanoparticles. A constellation of ten nanoparticles was used for the experiment described in this paper, yielding an achievable centroid localization precision value of $L_c = 0.13$ nm. Since displacement measurements are simply two centroid position measurements in the same coordinate frame, the localization precision values of the two position measurements add in quadrature, yielding 0.18 nm.

IV. EXPERIMENTAL DETAILS

A. Actuator Fabrication

A scratch drive actuator [2] was fabricated through a commercially available three-layer polysilicon thin-film micromachining process [34], chemically released from the phosphosilicate glass sacrificial mold by wet chemical etching, and untethered from the fabrication substrate by mechanical probing [3]. The actuator was 55-μm long and 120-μm wide, with a plate thickness of 1.5 μm and a bushing height of 1.5 μm.

The power-delivery circuit for the actuator consisted of interdigitated metal electrodes patterned on oxidized silicon substrates, with an insulating coating of zirconium dioxide that provided a high-impedance dielectric coupling between the electrodes and the devices. The circuit was fabricated according to a protocol that differs only slightly from that presented elsewhere [20]. After fabrication, the circuit was treated with a hydrophobic self-assembled monolayer coating of perfluorooctyltrichlorosilane by vacuum evaporation to enhance its surface properties and prevent absorption of atmospheric water vapor into the otherwise hygroscopic zirconium dioxide material.

B. Nanoparticle Deposition

Spherical carboxylate-modified polystyrene nanoparticles loaded with fluorescent dye molecules with excitation and emission peaks at 505 and 515 nm, respectively, were used as fluorescent labels. The nanoparticles had diameters of (210 $\pm$ 10) nm (average $\pm$ standard deviation) as specified by the manufacturer. The nanoparticles were deposited onto the released scratch drive actuator by microtargeted contact deposition as follows. The nanoparticles were diluted in deionized water to a concentration of approximately 10^8 particles/mL, and the resulting dispersion was loaded into a micromanipulator-mounted micropipette with a tip diameter of 10 μm. The micropipette

was connected to an air syringe, and its tip was lowered into contact with a glass microscope slide. The air syringe was loaded into a syringe pump, which was activated until the pressure in the syringe was great enough to cause fluid to begin flowing onto the glass slide. At this time, the syringe pump was stopped and the micropipette tip was raised out of contact with the slide. This action stopped the flow of liquid. The micropipette tip was then positioned above the targeted region of the microactuator by adjusting the micromanipulator. A percussive tap on the base of the micromanipulator was sufficient to bring the micropipette into brief contact with the microactuator, thereby depositing a small volume of liquid. The liquid evaporated in less than a second, leaving behind a cluster of nanoparticles with a convex diameter of approximately 50 μm. The microactuator was then loaded onto the surface of the power-delivery circuit by vacuum microprobe [20].

C. Environmental Control

The packaged power-delivery circuit described in Section IV-A was mounted onto a printed circuit board, which was installed on the fluorescence microscope stage within an incubator that held the surrounding temperature at 27.0 °C to stabilize the optics. Ultrahigh purity nitrogen was passed through a humidity controller and then over the surface of the power delivery circuit. An analog electronic hygrometer, integrated onto the printed circuit board 1 cm from the edge of the power delivery circuit, reported the local relative humidity. The humidity controller was adjusted until the reported value stabilized to within $\pm 1.2\%$ of 7.7% RH. The entire system was then allowed to stabilize for an hour before the start of the experiment.

D. Operation of the Scratch Drive Actuator

The electrical waveform used to power the scratch drive actuator in this experiment consisted of one 60-μs 130-V pulse issued every 3 s over a baseline voltage of 20 V, applied to the interdigitated electrodes of the power delivery circuit. When a signal is applied between adjacent pairs of electrodes on the power-delivery circuit, the voltage induced on the actuator is approximately half the signal voltage, regardless of the position of the actuator on the electrodes [3]. The equivalent voltage between the actuator and the underlying electrodes was therefore approximately 75 V during the pulses and 10 V at the baseline. The polarity of the waveform was reversed every 15 s, as discussed in the literature [20], to reduce parasitic charging within the dielectric layer above the electrodes. A desktop computer controlled the generation of a low-voltage representation of the waveform through a digital signal generator with a resolution of 1.25 megasamples/s. The output of the signal generator was amplified through a high-voltage power amplifier with a large-signal bandwidth of 250 kHz and a gain of 100 to achieve the desired voltages.

E. Image Collection

The fluorescent nanoparticles deposited on the microactuator were imaged with an inverted optical video microscope oper-

ated in widefield epifluorescence mode. A metal halide short arc lamp was used in conjunction with a 450–490-nm bandpass filter for fluorescence excitation, and a 495-nm dichroic mirror was used with a 500–550-nm bandpass emission filter to isolate fluorescence emission. An apochromatic air-immersion microscope objective lens with a magnification of $100\times$ and a numerical aperture of 0.95 was employed. The depth of field was estimated to be 0.8 μm. Images were collected by a 5-megapixel CCD camera with 36-bit RGB color depth. The data rate required of the camera was reduced by specifying a region of interest (ROI) that included a 15-μm-diameter constellation of nanoparticles. Prior to execution of the experiment, the microscope was manually focused to the best ability of the operator, and the exposure time of the camera was set to 300 μs, which was between 25% and 50% below image saturation. A series of nine fluorescence micrographs of the actuator was then collected with focal distances spaced at 200 nm increments centered about the initial manually determined value. The focal distance to be used for the experiment was chosen to be the distance of the test series image in which the normalized image of a fluorescent nanoparticle had the narrowest diameter. During the experiment, images were captured at $2/3$ frames/s, which was twice the stepping frequency of the scratch drive actuator, so that two images were taken at each position of the device under test. A total of 1000 images were collected from 500 different positions of the actuator.

F. Image Analysis

The green channel was extracted from the collected RGB images, whereas the red and blue channels were discarded to increase the signal-to-noise ratio of the data. A constellation of nanoparticles in the image series was selected for analysis, and the position of each particle in the constellation was calculated according to the three-step method described in Section II-B:

Step 1: morphological feature detection;
Step 2: two-point analytical estimation;
Step 3: nonlinear least squares regression analysis.

In **Step 1**, features in the image that potentially denoted the presence of nanoparticles were detected with a simple threshold method. The threshold value above which pixels in the image were included as potential targets was calculated from the expression $t = k(m - b) + b$, where t is the threshold value, $k = 4$ is an adjustable constant, m is the maximum pixel intensity in the image, and b is the background intensity of the image. Since the fluorescence micrographs in this measurement were sparsely populated with targets, as shown in Fig. 3, the background intensity could be easily sampled.

Pixels that surpassed the threshold intensity were asserted in a binary image mask, which was then filtered by area opening [35] so that only connected components containing at least nine pixels remained. An eight-connected neighborhood was used for the opening operation. The bounding boxes of all connected components remaining in the mask defined the ROIs for the next two steps of the process.

In **Step 2**, an initial Gaussian estimate of the point spread function was quickly calculated for each ROI from values

This article has been accepted for inclusion in a future issue of this journal. Content is final as presented, with the exception of pagination.

8   JOURNAL OF MICROELECTROMECHANICAL SYSTEMS

computed during morphological feature detection according to the following equation:

$$G = A \cdot e^{-((x-\hat{x})^2+(y-\hat{y})^2)/2\sigma^2} + C \tag{3}$$

where $(\hat{x}, \hat{y})$ are the coordinates of the peak, A is the peak height, σ^2 is the function variance, and C is the function offset. The initial estimate of the parameters, $\vec{P}_G = (A_1, \sigma_1, \hat{x}_1, \hat{y}_1, C_1)$, was chosen so that A_1 was the maximum background-adjusted pixel intensity in the ROI, $(\hat{x}_1, \hat{y}_1)$ were the coordinates of a maximum-intensity pixel in the ROI, and $C_1 = b$ was the background intensity of the image. The value of σ_1 was estimated from the size of the ROI bounding box $(w \times h)$ and the threshold value t as follows:

$$\sigma_1 = \frac{(w + h + 2)}{4\sqrt{4 \ln\left((A_1 + C_1)/(t - C_1)\right)}}. \tag{4}$$

This initial analytic approximation for the function parameters proved to be quite accurate in practice, typically exhibiting RMS error that fell within a factor of 10 of the best fit.

In **Step 3**, the initial estimates of the parameter values were refined to a least squares optimum by regression analysis using the Levenberg–Marquardt algorithm [36]. Termination tolerances used for single-iteration changes in the parameters and in the sum of squared residuals were both 10^{-6}. Termination usually occurred due to stabilization of the parameter estimates. Upon termination of the algorithm, the RMS error for a typical ROI was around 0.07. Although the parameters were not explicitly scaled prior to optimization, the initial estimation of Step 2 generally found the optimum peak position to within a pixel, making the search range of pixel-denominated parameters appropriate for the intensity-denominated parameters, which were normalized.

V. CONCLUSION

Super-resolution fluorescence microscopy has been used to measure the translations and rotations of a MEMS device in motion across a surface with standard uncertainties of 1.85 nm and 100 μrad, respectively. The measurement technique enabled observation of the individual stepwise displacements and rotations of a scratch drive actuator, which have not been observed previously. The motion of the actuator was characterized by highly localized transient variations in step size, which are not predicted by existing models of scratch drive behavior.

The data obtained from this type of measurement can be used to understand and optimize the kinematics of MEMS devices and for fundamental studies of the underlying surface forces, wear, and tribology at small length scales. The nanometer and submilliradian (or better) uncertainties of super-resolution fluorescence microscopy, combined with its broad compatibility with dry, wet, and vacuum environments, make it a powerful technique that will have broad impact in MEMS, NEMS, microrobotic automation, and nanomanufacturing.

The measurements reported here may be improved upon in several ways. First, stationary reference nanoparticles may be deposited within the field of view of the microscope to eliminate limitations of microscope stage vibration and drift,

which are suspected to be the primary contributor to the difference between the measured uncertainty and the calculated localization precision. Second, fluorescent point sources that do not satisfy the Rayleigh resolution criterion may be discriminated spectrally or temporally [37]–[39] to localize MEMS and NEMS devices in nanometer-scale proximity. Third, as determined by the size and operation of a device, constellations of fluorescent nanoparticles of optimized diameter and density may be placed by improved deposition methods such as inkjet printing to reduce measurement uncertainties.

REFERENCES

[1] D. A. Wang, F. W. Sheu, and Y. S. Chiu, "In-plane vibration characterization of microelectromechanical systems using acousto-optic modulated partially incoherent stroboscopic imaging," *Opt. Lasers Eng.*, vol. 49, no. 7, pp. 954–961, Jul. 2011.
[2] T. Akiyama, D. Collard, and H. Fujita, "Scratch drive actuator with mechanical links for self-assembly of three-dimensional MEMS," *J. Microelectromech. Syst.*, vol. 6, no. 1, pp. 10–17, Mar. 1997.
[3] B. R. Donald, C. G. Levey, C. D. McGray, D. Rus, and M. Sinclair, "Power delivery and locomotion of untethered microactuators," *J. Microelectromech. Syst.*, vol. 12, no. 6, pp. 947–959, Dec. 2003.
[4] E. E. Flater, A. D. Corwin, M. P. de Boer, and R. W. Carpick, "In situ wear studies of surface micromachined interfaces subject to controlled loading," *Wear*, vol. 260, no. 6, pp. 580–593, Mar. 2006.
[5] G. Subhash, A. D. Corwin, and M. P. de Boer, "Evolution of wear characteristics and frictional behavior in MEMS devices," *Tribol. Lett.*, vol. 41, no. 1, pp. 177–189, Jan. 2011.
[6] B. Bhushan, "Nanotribology and nanomechanics in nano/biotechnology," *Philos. Trans. Roy. Soc. A—Math. Phys. Eng. Sci.*, vol. 366, no. 1870, pp. 1499–1537, May 2008.
[7] D. M. Freeman, "Measuring motions of MEMS," *MRS Bull.*, vol. 26, no. 4, pp. 305–306, Apr. 2001.
[8] B. Serio, J. J. Hunsinger, and B. Cretin, "In-plane measurements of microelectromechanical systems vibrations with nanometer resolution using the correlation of synchronous images," *Rev. Sci. Instrum.*, vol. 75, no. 10, pp. 3335–3341, Oct. 2004.
[9] P. Sandoz, J. M. Friedt, and E. Carry, "In-plane rigid-body vibration mode characterization with a nanometer resolution by stroboscopic imaging of a microstructured pattern," *Rev. Sci. Instrum.*, vol. 78, no. 2, pp. 023706-1–023706-9, Feb. 2007.
[10] K. L. Ekinci, "Electromechanical transducers at the nanoscale: Actuation and sensing of motion in nanoelectromechanical systems (NEMS)," *Small*, vol. 1, no. 8/9, pp. 786–797, Aug. 2005.
[11] A. A. Trusov and A. M. Shkel, "Capacitive detection in resonant MEMS with arbitrary amplitude of motion," *J. Micromech. Microeng.*, vol. 17, no. 8, pp. 1583–1592, Aug. 2007.
[12] F. M. Dickey, S. C. Holswade, L. A. Hornak, and K. S. Brown, "Optical methods for micromachine monitoring and feedback," *Sens. Actuators A, Phys.*, vol. 78, no. 2/3, pp. 220–235, Dec. 14, 1999.
[13] Y. Zhong, G. Zhang, C. Leng, and T. Zhang, "A differential laser Doppler system for one-dimensional in-plane motion measurement of MEMS," *Measurement*, vol. 40, no. 6, pp. 623–627, Jul. 2007.

[14] D. Teyssieux, S. Euphrasie, and B. Cretin, "MEMS in-plane motion/vibration measurement system based CCD camera," *Measurement*, vol. 44, no. 10, pp. 2205–2216, Dec. 2011.

[15] G. Y. Zhou and F. S. Chau, "Grating-assisted optical microprobing of in-plane and out-of-plane displacements of microelectromechanical devices," *J. Microelectromech. Syst.*, vol. 15, no. 2, pp. 388–395, Apr. 2006.

[16] N. Bobroff, "Position measurement with a resolution and noise-limited instrument," *Rev. Sci. Instrum.*, vol. 57, no. 6, pp. 1152–1157, Jun. 1986.

[17] J. W. Lichtman and J. A. Conchello, "Fluorescence microscopy," *Nat. Methods*, vol. 2, no. 12, pp. 910–919, Dec. 2005.

[18] T. A. Berfield, H. K. Patel, R. G. Shimmin, P. V. Braun, J. Lambros, and N. R. Sottos, "Fluorescent image correlation for nanoscale deformation measurements," *Small*, vol. 2, no. 5, pp. 631–635, May 2006.

[19] G. T. A. Kovacs, *Micromachined Transducers Sourcebook*. New York: McGraw-Hill, 1998.

[20] B. R. Donald, C. G. Levey, C. D. McGray, I. Paprotny, and D. Rus, "An untethered, electrostatic, globally controllable MEMS micro-robot," *J. Microelectromech. Syst.*, vol. 15, no. 1, pp. 1–15, Feb. 2006.

[21] A. T. K. Hayakawa and A. Ueda, "An analysis of the elastic deformation of an electrostatic microactuator," *Trans. Inst. Elect. Eng. Jpn.*, vol. 188-E, no. 3, pp. 205–211, 1998.

[22] L. J. Li, J. G. Brown, and D. Uttamchandani, "Study of scratch drive actuator force characteristics," *J. Micromech. Microeng.*, vol. 12, no. 6, pp. 736–741, Nov. 2002.

[23] L. Li, J. G. Brown, and D. Uttamchandani, "Flexing of scratch drive actuator plates: Modelling and experimentation," *Proc. Inst. Elect. Eng.—Sci. Meas. Technol.*, vol. 151, no. 3, pp. 137–141, May 2004.

[24] E. Dumsong, N. Afzulpurkar, and A. Tuantranont, "Design, analytical modeling, and simulation of wire-free walking scratch-drive microrobot," *IEEE Trans. Ind. Electron.*, vol. 56, no. 4, pp. 1109–1120, Apr. 2009.

[25] P. Honarmandi, J. W. Zu, and K. Behdinan, "Analytical study and design characteristics of scratch drive actuators," *Sens. Actuators A, Phys.*, vol. 160, no. 1/2, pp. 116–124, May 2010.

[26] S. Chen, C. Chang, and W. Hsu, "Improved model of rectangular scratch drive actuator," *J. Micro-Nanolithography Mems Moems*, vol. 10, no. 1, p. 013016, Jan.–Mar. 2011.

[27] J. W. Zu, Q. Z. Qu, and G. Cheng, "Analytical modeling and quantitative analysis of scratch drive actuator," in *Proc. ICMENS*, 2004, pp. 629–635.

[28] P. Langlet, D. Collard, T. Akiyama, and H. Fujita, "A quantitative analysis of scratch drive actuation for integrated X/Y motion system," in *Proc. TRANSDUCERS*, 1997, pp. 773–776.

[29] M. Yu, X. Wang, M. Xie, G. Wang, and M. Zhang, "Analytical model of the electrostatic scratch drive actuator," in *Proc. Int. Symp. High Density Packag. Microsyst. Integr.*, 2007, pp. 1–4.

[30] P. J. Besl and N. D. McKay, "A method for registration of 3-D shapes," *IEEE Trans. Pattern Anal. Mach. Intell.*, vol. 14, no. 2, pp. 239–256, Feb. 1992.

[31] R. J. Linderman and V. M. Bright, "Nanometer precision positioning robots utilizing optimized scratch drive actuators," *Sens. Actuators A, Phys.*, vol. 91, no. 3, pp. 292–300, Jul. 2001.

[32] Technical Advisory Group W. G. I.S.O., International Standards Organization, Geneva, Switzerland, Guide to the Expression of Uncertainty in Measurement, 1995.

[33] K. I. Mortensen, L. S. Churchman, J. A. Spudich, and H. Flyvbjerg, "Optimized localization analysis for single-molecule tracking and super-resolution microscopy," *Nat. Methods*, vol. 7, no. 5, pp. 377–381, May 2010.

[34] K. W. Markus, D. A. Koester, A. Cowen, R. Mahadevan, V. R. Dhuler, D. Roberson, and L. Smith, *MEMS Infrastructure: The Multi-User MEMS Processes (MUMPs)*. Bellingham, WA: SPIE, 1995.

[35] A. Meijster and M. H. F. Wilkinson, "A comparison of algorithms for connected set openings and closings," *IEEE Trans. Pattern Anal. Mach. Intell.*, vol. 24, no. 4, pp. 484–494, Apr. 2002.

[36] D. W. Marquardt, "An algorithm for least-squares estimation of nonlinear parameters," *J. Soc. Ind. Appl. Math.*, vol. 11, no. 2, pp. 431–441, Jun. 1963.

[37] S. T. Hess, T. P. K. Girirajan, and M. D. Mason, "Ultra-high resolution imaging by fluorescence photoactivation localization microscopy," *Biophys. J.*, vol. 91, no. 11, pp. 4258–4272, Dec. 2006.

[38] M. J. Rust, M. Bates, and X. W. Zhuang, "Sub-diffraction-limit imaging by stochastic optical reconstruction microscopy (STORM)," *Nat. Methods*, vol. 3, no. 10, pp. 793–796, Oct. 2006.

[39] A. Pertsinidis, Y. Zhang, and S. Chu, "Subnanometre single-molecule localization, registration and distance measurements," *Nature*, vol. 466, no. 7306, pp. 647–651, Jul. 29, 2010.

Craig D. McGray, photograph and biography not available at the time of publication.

Samuel M. Stavis, photograph and biography not available at the time of publication.

Joshua Giltinan, photograph and biography not available at the time of publication.

Eric Eastman, photograph and biography not available at the time of publication.

Samara Firebaugh, photograph and biography not available at the time of publication.

Jenelle Piepmeier, photograph and biography not available at the time of publication.

Jon Geist, photograph and biography not available at the time of publication.

Michael Gaitan, photograph and biography not available at the time of publication.